Nuclear Science and Techniques (2026) 37:19
https://doi.org/10.1007/s41365-025-01840-y

Emittance optimization of gridded thermionic-cathode electron gun for high-quality beam injectors

Xiao-Yu Peng[1] · Hao Hu[2] · Tong-Ning Hu[2] · Jian Pang[1] · Jian-Jun Deng[3] · Guang-Yao Feng[1]

Received: 9 July 2024 / Revised: 25 August 2024 / Accepted: 9 September 2024 / Published online: 9 December 2025

Abstract
Electron beam injectors are pivotal components of large-scale scientific instruments, such as synchrotron radiation sources, free-electron lasers, and electron-positron colliders. The quality of the electron beam produced by the injector critically influences the performance of the entire accelerator-based scientific research apparatus. The injectors of such facilities usually use photocathode and thermionic-cathode electron guns. Although the photocathode injector can produce electron beams of excellent quality, its associated laser system is massive and intricate. The thermionic-cathode electron gun, especially the gridded electron gun injector, has a simple structure capable of generating numerous electron beams. However, its emittance is typically high. In this study, methods to reduce beam emittance are explored through a comprehensive analysis of various grid structures and preliminary design results, examining the evolution of beam phase space at different grid positions. An optimization method for reducing the emittance of a gridded thermionic-cathode electron gun is proposed through theoretical derivation, electromagnetic-field simulation, and beam-dynamics simulation. A 50% reduction in emittance was achieved for a 50 keV, 1.7 A electron gun, laying the foundation for the subsequent design of a high-current, low-emittance injector.

Keywords Electron gun · Gridded · Beam injector · Beam dynamics · Emittance optimization

1 Introduction

Electron beam injectors in accelerator facilities, such as synchrotron radiation sources [1], free-electron lasers (FEL), and electron-positron colliders [2, 3], play a crucial role in generating, accelerating, and focusing high-performance electron beams. The overall performance of the device depends largely on the quality of the driving electron beam provided by the injector, and the initial electron beam generated by the electron gun largely determines the performance limit of the injector and even the entire device [4]. Therefore, large scientific research facilities based on accelerators have strict requirements regarding the quality of injectors, especially electron guns [5–7].

Common methods of electron emission from electron gun cathodes include photoelectric, field, and thermal emissions [8–10]. Electron extraction and acceleration typically involve the use of either direct-current (DC) high voltage or radio-frequency (RF) high voltage [11–13]. Electron guns commonly used for FEL and synchrotron radiation include photocathode RF electron guns [14] and thermionic-cathode high-voltage electron guns. The former requires a costly laser system with complex operation and maintenance, whereas the thermionic-cathode injector has a simple structure, affordability, high power and current output capabilities, and long-term stable operation [15, 16]. The gridded thermionic-cathode electron gun offers flexible beam-quality control through the grid. By regulating the beam emission

This work was supported by the Hundred-person Program of Chinese Academy of Sciences and the National Natural Science Foundation of China (No.11905074).

✉ Tong-Ning Hu
TongningHu@hust.edu.cn

✉ Guang-Yao Feng
fenggy@ustc.edu.cn

[1] National Synchrotron Radiation Laboratory, University of Science and Technology of China, Hefei 230029, China

[2] State Key Laboratory of Advanced Electromagnetic Technology, School of Electrical and Electronic Engineering, Huazhong University of Science and Technology, Wuhan 430074, China

[3] Institute of Fluid Physics, Chinese Academy of Engineering Physics, Mianyang 621000, China

via the grid, wear on the components of the gun is minimized and thermal expansion is reduced, thereby extending the operational lifetime of the electron gun [17].

Gridded thermionic-cathode electron guns have been employed in various global projects. For instance, Asaka et al. developed a low-emittance RF electron gun system using a gridded thermionic cathode for a 1 GeV storage ring NewSUBARU injector, demonstrating stable operation. The system comprises an electron gun operating at 50 kV, a 238 MHz RF accelerating cavity, and solenoids. It offers notable advantages, including compact size, low emittance, and high stability [18]. The injector for Beijing's fourth-generation synchrotron radiation source, the High Energy Photon Source [19], incorporates a gridded thermionic-cathode electron gun. The linear accelerator achieves an output beam energy of 500 MeV and a macro pulse repetition rate of 50 Hz. The electron gun is capable of delivering a bunch charge of up to 10 nC [20].

However, the beam energy generated by conventional gridded thermionic-cathode electron guns is limited by significant space charge effects [21–23], resulting in excessive emittance. This limitation significantly affects the design and optimization of subsequent facilities. Therefore, it is important to use the RF field to rapidly accelerate the output electron beam of the gun to offset these space charge forces. The electron gun primarily comprises a cathode, focusing structure, and anode [24]. A gridded electron gun involves adding a grid near the cathode surface of a conventional gun, which is set to the same potential as that of the focusing structure. This configuration controls the emission timing of the electron beam and optimizes its initial quality [25]. Structural modifications in the electron gun alter the electric field, thereby influencing the quality of the emitted beam. Simulation and iterative optimization of the design are necessary to ensure that the emitted beam current meets the requirements of the subsequent accelerator facilities.

This study focuses on optimizing a gridded electron gun. Using the CST Studio Suite, we simulated the electron beam drift under electric field effects and optimized the key parameters to achieve high-quality electron beam currents. The optimization of key parameters, such as the grid type, wire spacing, grid bias voltage, and other structural aspects, is conducted by analyzing the transverse phase space [26] information of the beam near the grid. To verify the applicability of the electron gun to subsequent facilities, a subharmonic bunching (SHB) cavity was added to accelerate the electron beam [2], and solenoids were added to compensate for the emittance. This scheme aims to achieve a low-emittance and high-quality electron beam output. Based on the injector structure in Japan, an electron gun model was developed using the Tracking solver within CST. A negative high voltage is applied to the cathode, while the anode is grounded, causing electrons to be emitted across the cathode surface barrier and accelerated toward the anode port by the electric field between them [27]. This setup resulted in an extremely low emittance at the exit of the electron gun system. The last section discusses the scheme of using a SHB to accelerate and solenoids to constrain the electron beam at the exit of the electron gun system [28], along with the electron beam current parameters at the final beam waist position.

2 Brief review of previous design for electron Gun

The development of an electron gun system that generates high-quality, low-emittance beams is of paramount importance for achieving breakthroughs in the key technology of free-electron laser (FEL) injectors. This section provides a detailed discussion of the electron gun system design, which includes the cathode, grid, focusing structure, and anodes. The cathode operates at a high voltage of -50 kV, with a specific voltage difference set between the grid and cathode, known as the grid bias voltage. The focusing structure and grid were maintained at equipotential, whereas the anode was grounded.

In the simulation studies of a previous publication, we designed an electron gun with a cathode emission surface radius (r_{cathode}) of 3.5 mm, and the normalized emittance of the electron beam at the exit was 2 mm mrad [29]. The current intensity of the electron beam obtained by the electron gun of this structure is 1.5 A, and a higher current intensity of 1.7 A is desired. According to the emission capacity of the cathode, the larger the size of the cathode, the higher the current intensity, so we expand r_{cathode} to 4 mm. However, this results in an emittance increase to 2.5 mm mrad. Therefore, further structural optimization is necessary to reduce emittance. Drawing from previous design experience of electron guns, the tilt angle of the focusing electrode is adjusted to 57°, the height to 7.5 mm and the anode-cathode distance is set to 16 mm to achieve a beam characterized by a higher laminar flow pattern and lower emittance. The optimized structure of the electron gun and beam trajectory obtained from the CST simulations are shown in Fig. 1a. From this figure, it can be seen that the beam waist is very long and the beam-spot size at 40 mm after the anode outlet does not change much compared with the beam-spot size at the anode outlet, which indicates that the beam has good laminar flow.

In previous electron gun models simulated using CST, various mesh shapes, including honeycomb, spoke, and orthogonal configurations [30], were investigated, as shown in Fig. 1b. According to the preliminary results, the spoke-wheel grid exhibited the lowest emission efficiency. The orthogonal and honeycomb grids resulted in comparable

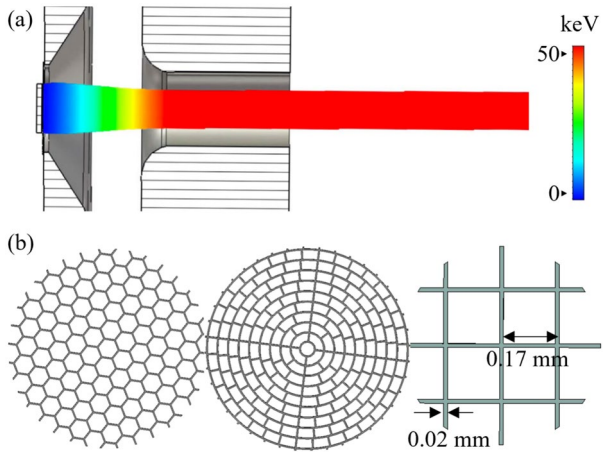

Fig. 1 (Color online) **a** Electron gun structure and electron beam energy distribution characteristics. **b** The structure diagram of different grids (including honeycomb, rectangular, spoke)

beam qualities, with the orthogonal grid being easier to fabricate than the honeycomb grid [29]. Therefore, from an engineering implementation perspective, this study adopts an orthogonal grid structure. The Tracking solver within the particle tracking module of CST software is utilized to achieve an emission current of 1.7 A at the exit of electron gun using the Fix emission mode. The width ratio between the analysis mesh and wires was set to 1:2 to meet the accuracy requirements of the simulation.

To achieve a higher beam quality, selecting an appropriate cathode material is essential to provide larger emission currents from a smaller emitting area. Rare earth hexaborides (RB_6), such as cerium hexaboride (CeB_6), possess unique characteristics, including high hardness, high melting point, low work function, good chemical stability, and resistance to ion bombardment [31, 32]. Among various RB_6 materials, CeB_6 exhibits lower evaporation rates, higher electrical resistivity, and longer lifetimes [33]. In this study, a CeB_6 planar cathode with an emission surface radius of 4 mm was chosen, which theoretically meets the requirements for emission current density. The application of CeB_6 cathodes in facilities such as Spring-8 FEL has confirmed their reliability [34, 35].

A model of the cathode was established in CST, and subsequently, a grid structure was integrated behind it, with the configuration of the cathode and grid structure being optimized and analyzed. Based on the aforementioned simulation model, it is crucial to investigate the influence of the voltage difference between the grid and cathode on beam emittance. The variation in emittance with bias voltage is illustrated in Fig. 2a. The beam emittance initially decreased and then gradually increased as the bias voltage increased, reaching a minimum at a grid bias voltage of approximately 320 V. At lower bias voltages, the insufficient electric field

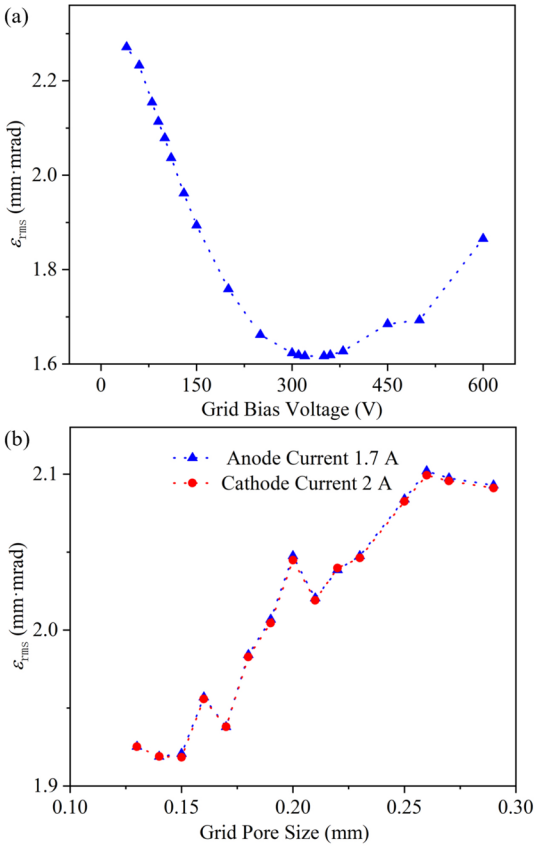

Fig. 2 **a**The emittance varies with voltage difference. **b** The emittance varies with the spacing between wires

between the cathode and grid leads to a larger beam emittance. As the absolute value of the bias voltage increased, the laminarity of the beam improved, resulting in enhanced emittance performance. However, beyond a certain threshold, an increase in emittance can be caused by further increasing the bias voltage.

The spacing between the wires and the wire width significantly affects the beam quality. Simulations are conducted to compare grids with wire widths of 0.02 mm, 0.03 mm, and 0.04 mm. Table 1 shows that finer wires result in higher electron transmission rates, but thinner wires are prone to deformation and increase in manufacturing difficulty. Therefore, it is recommended to choose a wire with a width of 0.02 mm. The simulation and calculation of the effect of

Table 1 The beam transmission rate varies with the width of the wire

Wire size (mm)	Particle transmission rate (%)
0.02	90
0.03	74
0.04	68

spacing between wires on emittance were performed using two methodologies: one by setting the cathode output current to 2 A, and the other by maintaining the current at the anode outlet position to 1.7 A. Figure 2b illustrates that within a specific range of wire spacing, the emittance tends to increase with larger wire spacing. The emittance tends to be stable around 2.1 mm mrad when the wire spacing exceeds 0.26 mm. In addition, when the wire spacing is less than 0.15 mm, the emittance is stable at about 1.9 mm mrad. Therefore, within the range of wire spacing from 0.15 mm to 0.26 mm, it is observed that smaller wire spacing varies with lower emittance levels. Notably, under the two setting conditions, a consistent inflection point appeared at a wire spacing of 0.17 mm. The smaller the wire spacing, the more electrons are bombarded on the grid, and the more obvious the thermal deformation effect. A wire spacing of 0.17 mm not only reduces emittance but also enhances the beam transmission rate, improves cathode efficiency, and extends the lifetime of both the cathode material and the grid. Finally, the simulated electron gun achieved an acceleration gradient of less than 4 MV/m, resulting in a beam emittance of 1.3 mm mrad and a current intensity of 1.7 A (charge of 1 nC, pulse length of 600 ps).

3 Emittance optimization via grid re-configuration

The preceding section demonstrated that the beam emittance is significantly affected by the grid structure. Hence, further optimization of the grid structure is essential. During the electron gun simulations using the CST Studio Suite, 2D particle monitors were placed at positions where electrons passed through the grid and at the gun exit. Observations from these monitors revealed that the grid-induced field effects caused the electron beam spot to exhibit a consistent pattern aligned with the grid structure, as shown in Fig. 3. Yellow and blue dots represent electrons, and the circular pattern depicts the beam-spot image. Local amplification revealed the electron distribution, which demonstrated that the magnified beam spot displayed a distinct grid pattern. For the convenience of further study, particles on the stripes within y of 0 mm~0.17 mm need to be marked in blue.

3.1 Basic idea and theoretical analysis

In the realm of beam physics, the analysis of phase space (x–x' plane) provides a more intuitive understanding. The analysis of the position and momentum within each phase space cell enables the exploration of their relationship with the overall emittance.

The emittance of a beam is quantified by the area of the phase-space ellipse. In addition to geometrical

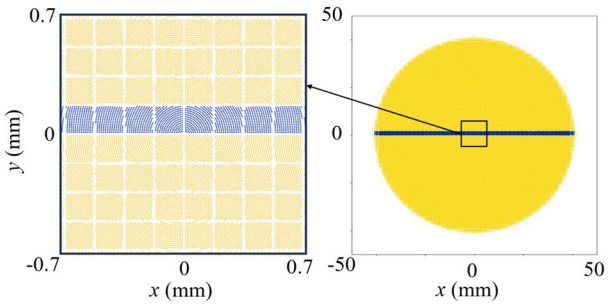

Fig. 3 (Color online) The simulation result of the particle beam spot, including detailed magnifications, is presented for a position 0.8 mm behind the grid. (Yellow and blue dots represent electrons, with the blue dot specifically denoting the electron selected for subsequent analysis.)

explanations, emittance can be described statistically by assessing the dispersion of all particles in the x-x' phase space.

The RMS emittance ε can be defined by the following Eq. (1) [36]:

$$\varepsilon^2 = \frac{1}{n^2}\sum_{i=1}^{n}(x_i-\bar{x})^2\cdot\sum_{i=1}^{n}(x_i'-\bar{x'})^2 - \frac{1}{n^2}\Big[\sum_{i=1}^{n}(x_i-\bar{x})\cdot(x_i'-\bar{x'})\Big]^2. \tag{1}$$

Because the beam-spot cross section can be considered as composed of individual grid cells, the transverse phase space of the beam can also be decomposed into transverse phase spaces of multiple grid cells. Normalizing each cell's transverse phase space, represented as (x_i, x_i'), involves methods such as finding their centroids to yield a single point $(\bar{x}, \bar{x'})$. As shown in Fig. 4a and b, the phase-space information of each grid cell can be discretized using its emittance and normalized slope away from the centroid point. Here, Fig. 4a illustrates the representation of the grid phase space using the coordinates of n electrons, denoted by the four coordinate points $(a, 0), (a, k_1 a), (-a, 0), (-a, -k_1 a)$, where k_1 represents the normalized.

Thus, for the analysis of each grid's phase space, the emittance in Eq. (1) can be transformed into the following Eq. (2):

$$\varepsilon^2 = \frac{1}{n^2}(na^2)\left(\frac{n}{2}k_1^2a^2\right) - \frac{1}{n^2}\left(\frac{n}{2}k_1a^2\right)^2 = \frac{{k_1}^2a^4}{4}. \tag{2}$$

To achieve a more approximate and uniformly discretized distribution of electrons within each grid cell, for electrons of each grid, the center point in Fig. 4b is denoted as $(\bar{x}, \bar{x'})$, with scattered electron coordinates labeled as (a, b), $(2a, b)$,

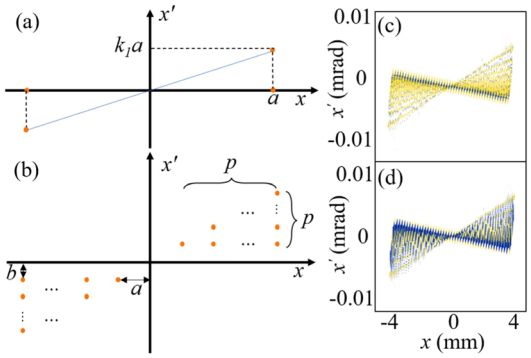

Fig. 4 (Color online) **a** The electrons are evenly separated from the normalized coordinate points to four coordinate points. **b** Electrons are uniformly dispersed from the normalized coordinate points to multiple regular coordinate points, and each coordinate point contains only one electron. The blue dots represent the fitted electron position, and the yellow dots represent the actual electron position. **c** Describe the comparison between the fitting obtained by the discrete method of (**a**) and the actual electronic phase space. **d** Describe the comparison between the fitting obtained by the discrete method of (**b**) and the actual electronic phase space

$(2a, 2b), \cdots, (pa, pb), (-a, -b), (-2a, -b), (-2a, -2b), \cdots, (-pa, -pb), b/a = k_1$.

Thus, the emittance Eq. (1) for each grid cell can be transformed into the following Eq. (3):

$$\begin{aligned}\varepsilon^2 &= \frac{4}{n^2}\sum_{i=1}^{p} i(ia)^2 \cdot \sum_{i=1}^{p}[p-(i-1)](ib)^2 \\ &\quad - \frac{4}{n^2}\left\{\sum_{j=1}^{p}\left[\sum_{i=1}^{j}(ja \cdot ib)\right]\right\}^2 \\ &= \frac{3p^4+6p^3-p^2-4p-4}{144}\cdot a^2b^2.\end{aligned} \tag{3}$$

Figure 4c and d demonstrates the fitting of this method to phase space. Evidently, the two fitting methods are well aligned and can be utilized for subsequent simplified calculations.

The normalized slope of the overall transverse phase space of the beam spot is primarily determined by the electric field distribution between the cathode grids. The grid structure influences the electric field within each grid aperture, thereby altering the phase space of the beam, specifically, the transverse phase space of the grid. To simplify the phase-space information, as shown in Fig. 5, the blue line connecting the blue dots represents the overall transverse phase space of the beam spot, with each blue dot denoting a normalized point corresponding to each grid. The yellow dots represent discrete points obtained from the emittance and normalized slope of the grid. Thus, the area of the ellipse containing all the yellow dots represents the overall beam-spot emittance. As shown in Fig. 5a and b, it is evident

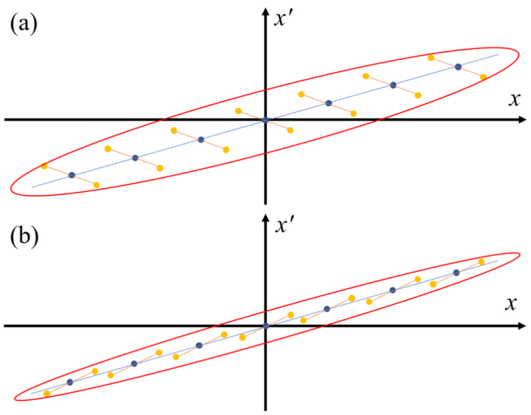

Fig. 5 The yellow line denotes the normalized slope of the beam across each small grid. The blue line represents the normalized slope of the entire beam spot. The absolute difference of slopes between the blue and yellow lines in (**a**) is greater than that in (**b**)

that as the slope of each grid approaches the overall slope, the beam-spot emittance decreases significantly.

Utilizing the emittance formula derivation shown in Fig. 6, consider a total of $8n_1$ electron composing the entire beam spot, divided into four grid cells, with $2n_1$ electrons in each cell. Assume the normalized position coordinates of electrons within each grid cell, as depicted by the blue dots in Fig. 6, are $(a, 0), (a, b), (-a, 0), (-a, -b)$. For this beam spot consisting of $8n$ electrons, the relationship for its emittance, derived using the method of least squares, yields a normalized slope of $b/2a$. The emittance relationship is given by:

$$\begin{aligned}\varepsilon^2 &= \frac{1}{(8n_1)^2}(8n_1a^2 \cdot 4n_1b^2) - \frac{1}{(8n_1)^2}(2n_1 \cdot 2ab)^2 \\ &= \frac{a^2b^2}{4}.\end{aligned} \tag{4}$$

Therefore, it is essential to examine the relationship between the normalized slope of the four grid units and the overall

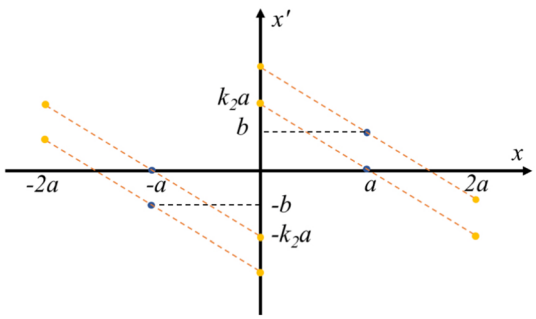

Fig. 6 Dispersing four blue coordinate points into eight yellow-coordinate points

normalized slope of the spot. As depicted in Fig. 4a, the blue coordinate points in Fig. 6 are discretized into yellow-coordinate points. For simplification of the calculation, the electron emittance within each grid was disregarded, focusing solely on the normalized slope. Each blue coordinate point was eventually discretized into two yellow points. Assuming a consistent normalized slope of k_2 for each small cell, the dispersed electron coordinates are: $(2a, b + k_2a)$, $(0, -k_2a + b)$, $(0, k_2a)$, $(-2a, -k_2a)$, $(0, -k_2a)$, $(2a, k_2a)$, $(-2a, -k_2a - b)$, $(0, k_2a - b)$, with n_1 particles at each coordinate point.

Thus, the emittance formula for each cell, Eq. (1) can be transformed as follows:

$$\begin{aligned}\varepsilon^2 &= \frac{1}{8^2}\cdot\left[4(2a)^2 + 2(k_2a+b)^2 + 2(-k_2a+b)^2 + 4k_2a^2\right] \\ &\quad - \frac{1}{8^2}\cdot\left[2a\cdot(k_2a+b) + 4k_2a^2 + 2a\cdot(k_2a+b)\right]^2 \\ &= a^4\cdot\left(k_2^2 - \frac{b}{a}k_2 + \frac{3b^2}{4a^2}\right).\end{aligned} \tag{5}$$

The overall emittance decreased when the slope of each grid cell closely approximated the overall normalized slope $b/2a$ of the beam spot. This provides a theoretical foundation for optimizing the emittance of gridded electron guns.

3.2 Beam emittance optimization

Based on the theoretical derivation and diagram in the previous section, the structure of the electron gun grid was optimized to enhance the beam emittance.

It is necessary to analyze the particles labeled in blue within the grid near the x-axis of the beam spot, as shown in Fig. 3. The normalized emittance slopes were calculated individually for 48 cells containing electrons, and their trajectories were tracked to assess their respective beam spots and phase spaces upon reaching the anode exit. The electron beam spot and transverse phase space are shown in Fig. 7, the color gradient from blue to purple indicates the distribution of the beam spot and transverse phase space of electrons. The electrons from the selected stripe of the beam spot are highlighted in orange, along with their transverse phase-space distribution. Figure 7(a) and (c) represents the electron information at 0.8 mm from the grid, whereas Fig. 7b and d shows the electron information at the electron gun exit, with purple and orange indicating the positions of the electron beam concentration. According to the transverse phase-space diagram, the normalized emittance slope of the overall beam spot was negative. The normalized beam emittance at the electron gun exit is 1.3 mm mrad (99.7% core part).

The normalized slopes of each grid cell within the yellow stripe shown in Fig. 7a are calculated, yielding the blue line around x in Fig. 8. It can be observed that all grid

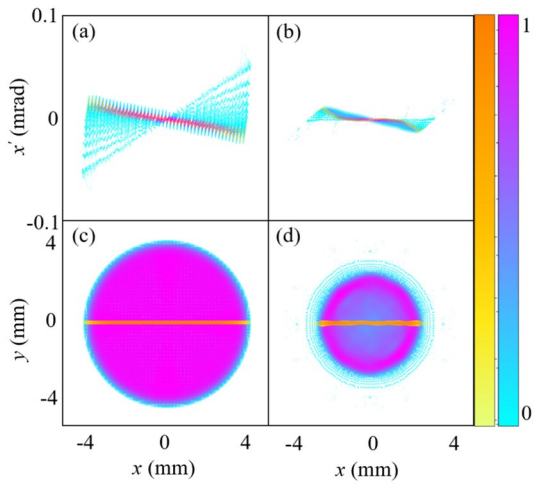

Fig. 7 (Color online) **a** Transverse phase-space diagram at a distance of 0.8 mm from the grid. **b** Transverse phase-space diagram at the anode exit position. **c** Beam-spot diagram at a distance of 0.8 mm from the grid. **d** Beam-spot diagram at the anode exit position

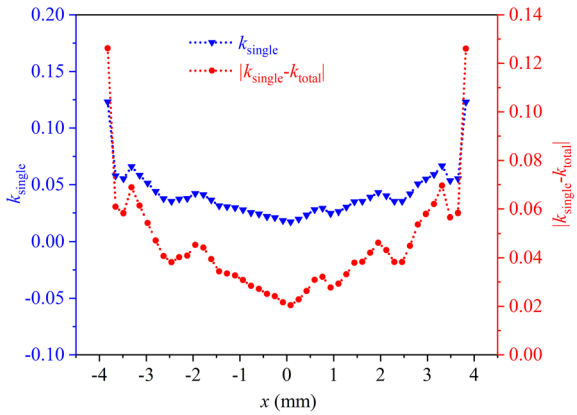

Fig. 8 The blue points represent the slope of particles within each grid near the grid. The red points represent the absolute difference in slope between the grid of small patches and the macro-bunch slope

cell slopes are positive. The absolute differences between these data points and the overall normalized slope of the large beam spot are depicted by the red curve. The red curve illustrates a notable disparity between the phase-space slope of an individual grid cell and the slope of the entire spot, particularly noticeable within the annular region of radius 2 mm~4 mm. Hence, to effectively decrease the slope of the edge grid unit and minimize the overall emittance, the external structure of the grid must be adjusted to alter the distribution of the electric field lines. Increasing the height of the grid edge relative to the center position and reducing the distance from the cathode to the perimeter of the grid can enhance the field strength, ultimately decreasing the slope of each grid.

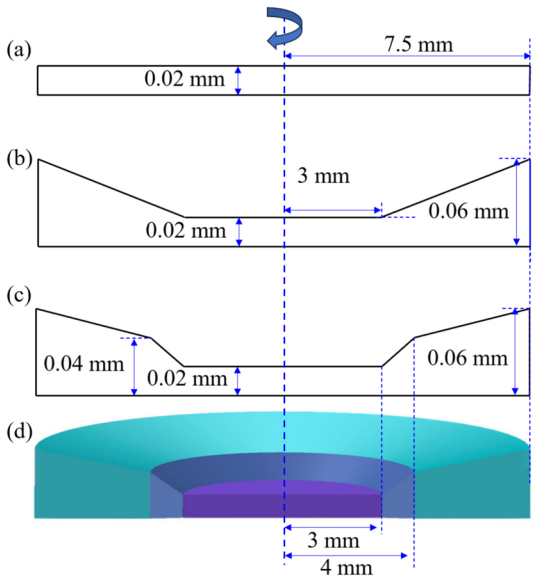

Fig. 9 (Color online) The schematic diagram illustrates the *yoz* cross section of the grid

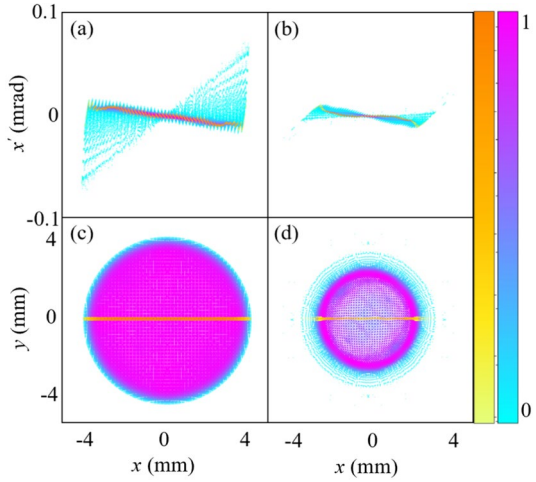

Fig. 10 (Color online) **a** Transverse phase-space diagram at a distance of 0.8 mm from the grid. **b** Transverse phase-space diagram at the anode exit position. **c** Beam-spot diagram at a distance of 0.8 mm from the grid. **d** Beam-spot diagram at the anode exit position

For the conventional grid structure, the *yoz* cross section shown in Fig. 9a appears rectangular. To achieve the desired optimization goals, the edges of the grid structure were elevated, as shown in Fig. 9b, resulting in a reduced beam emittance. Further optimization of the slopes was pursued, leading to the design shown in Fig. 9c, and a subsequent improvement in the emittance reduction. Figure 9d illustrates a three-dimensional view of the structural optimization results for grid thickness, as shown in Fig. 9c. These modifications enable the electric field structure to enhance the laminarity of the beam flow. The results near the grid and at the anode exit position regarding the beam spot and transverse phase space are shown in Fig. 10.

The normalized slopes of the particles within the yellow-marked grid cells shown in Fig. 10c are calculated, resulting in the blue curve depicted in Fig. 11. The absolute differences between these data points and the overall normalized slope of the large beam spot were computed to generate the red curve. The electron beam spot was symmetrical about the center of the circle. The number of each square-shaped spot increased along the radial direction and was proportional to the perimeter. Consequently, the slope differences at the varying radii, as depicted in Figs. 8 and 11, are weighted by the radius. The pre-optimization value is 2.47, while the post-optimization value is 1.44. The overall beam emittance can be reduced, and the beam emittance at the exit position of the electron gun can be reduced to 1.1 mm mrad (99.7% core part) as shown in Fig. 12.

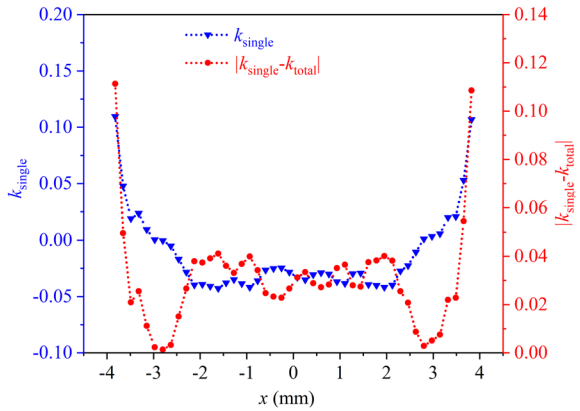

Fig. 11 The blue points represent the slope of particles within each grid near the grid. The red points represent the absolute difference in slope between the grid of small patches and the macro-bunch slope

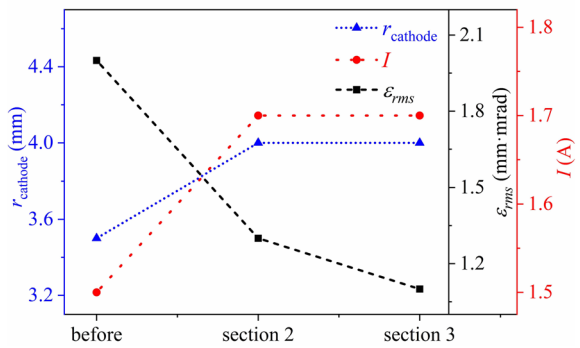

Fig. 12 Variations in beam current and emittance after optimization of Sect. 2 and Sect. 3

4 Further consideration with subsequent SHB

To verify the application of the optimized electron gun beam in subsequent components, simulation analyses were conducted using the CST Studio Suite. We designed a gridded thermionic RF accelerator system capable of emitting high-quality beam currents, which comprised a gridded electron gun, SHB, and solenoids. Beam dynamics simulations [14] and optimizations have been performed to achieve high-quality beam emission [37, 38].

The initial RF component in the injector system following the electron gun is an SHB. It is used for beam pre-bunching and acceleration and plays a crucial role in the injector setup. The SHB compresses the longitudinally uniform electron beam emitted by the electron gun and enhances the longitudinal electron density, which is crucial for the subsequent acceleration and focusing in the following accelerator section [39, 40]. The microwave field within the RF cavity is a time-varying standing wave field, necessitating the optimization of the cavity structure and phase tuning to achieve high-gradient acceleration and adequate focusing for subsequent stages of beam acceleration and focusing.

Introducing a solenoid in the beam transport process is similar to introducing a lens. It utilizes lensing to focus the electron beam, compensating for the space charge effects that affect the normalized transverse root-mean-square emittance on the x–x' plane. This lensing effect mitigates the growth in the projected emittance on the x–x' plane observed prior to focusing [41].

The beam energy at the exit of the electron gun is only 50 keV, which is much lower than the relativistic velocities. Consequently, the substantial space charge force among electrons causes rapid emittance growth during drift. Thus, minimizing the distance between the RF cavity and electron gun outlet is crucial. Here, the distance from the electron gun exit to the center of the RF cavity is set to 200 mm. Structural optimization of the RF cavity allows for the integration of a solenoid between the electron gun and RF cavity. Additionally, considering the future requirements for feeding other harmonic cavities and traveling wave tubes, another solenoid was added at the exit of the 238 MHz RF cavity. Optimization across these three components ensures that the normalized emittance of the beam reaches 1.5 mm mrad after a certain drift distance beyond the second solenoid, surpassing the typical emission levels of conventional thermionic electron gun injectors.

In CST simulations, when the electron beam reaches the RF cavity, its energy is 50 keV with a normalized root-mean-square emittance of 1.1 mm mrad. By adjusting the phase of the RF cavity to accelerate the electrons and considering the longitudinal focusing, the changes in the beam energy and transverse size after passing through the RF cavity are shown in Fig. 13. The figure also indicates the phase space at the exit of the RF cavity and the transverse phase space of the beam waist obtained from the overall structure of the RF cavity. Under the influence of the RF field, the beam energy increases by nearly a factor of ten, reaching 500 keV. The normalized root-mean-square emittance remained 1.5 mm mrad Table 2.

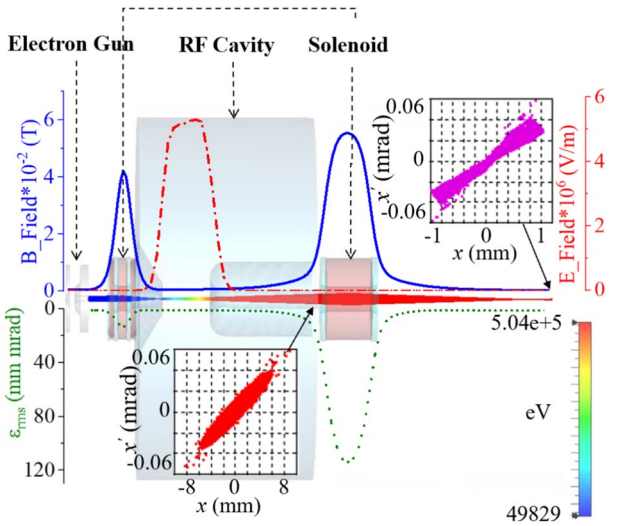

Fig. 13 (Color online) The trajectory and energy variation of the beam passing through the focusing solenoids and RF cavities. The red curve represents the axial electric field distribution generated by the RF cavity, and the blue curve represents the longitudinal distribution of the magnetic field generated by the solenoids. In the context of electron guns, the transverse emittance of the particle beam varies with longitudinal changes

Table 2 Beam parameters at the exit of the RF cavity before and after the optimization of the grid structure

Parameters	Original value	Optimized value
Current (A)	1.69	1.70
Energy (keV)	500	500
RMS emittance (mm mrad)	2.0	1.5

5 Conclusion

We designed, derived, and simulated a low-emittance, high-quality RF gridded thermionic electron gun system. Using the electron gun system model established in CST, information such as the emittance and current of the electron beam was analyzed. Considering that the grid structure has

a significant influence on the output of the electron gun, we analyzed and optimized this component in detail. First, we selected the appropriate grid shape and preliminarily optimized key parameters, such as the grid wire width, spacing, and grid bias voltage. Subsequently, the longitudinal structure of the grid was optimized. Specifically, we further analyzed the electron beam phase space of different grids through the grid and studied the influence on the overall emittance through data and theoretical analysis, formula derivation, and so on. Based on this, it is proposed to adjust the longitudinal length of the grid at different radius positions to reduce the electron beam emittance.

Ultimately, the electron gun designed is capable of emitting a beam current of 1.7 A, with the normalized emittance reduced by approximately 50% to 1.1 mm mrad, and beam-spot radius of 3 mm at the anode position. Furthermore, the exit of the electron gun is positioned at the shortest mechanical distance from the solenoid and RF cavity to facilitate beam focusing and acceleration. Beam dynamics simulation involves adjusting the structure, phase, and magnetic field intensities of these components. The beam can be accelerated to 500 keV over a short distance, achieving a normalized emittance of 1.5 mm mrad. In future work, we plan to process this grid structure and conduct emission experiments to evaluate its practical application.

Appendix

Eq. (3) can be derived from the following equation, where $n = p(p+1)$:

$$
\begin{aligned}
\varepsilon^2 &= \frac{1}{n^2}\sum_{i=1}^{n}(x_i-\bar{x})^2\cdot\sum_{i=1}^{n}(x_i'-\bar{x'})^2 \\
&\quad -\frac{1}{n^2}\Big[\sum_{i=1}^{n}(x_i-\bar{x})\cdot(x_i'-\bar{x'})\Big]^2 \\
&= \frac{4}{n^2}\sum_{i=1}^{p}i(ia)^2\cdot\sum_{i=1}^{p}[p-(i-1)](ib)^2-\frac{4}{n^2}\left\{\sum_{j=1}^{p}\left[\sum_{i=1}^{j}(ja\cdot ib)\right]\right\}^2 \\
&= \frac{4}{n^2}[a^2+2(2a)^2+3(3a)^2+\ldots+p(pa)^2]\cdot \\
&\quad [pb^2+(p-1)(2b)^2+(p-2)(3b)^2+\ldots+(pb)^2] \\
&\quad -\frac{4}{n^2}(ab+2a\cdot b+2a\cdot 2b+3a\cdot \\
&\quad b+3a\cdot 2b+3a\cdot 3b+\ldots+pa\cdot pb)^2 \\
&= \frac{4}{n^2}(1^3a^2+2^3a^2+\ldots+p^3a^2)\cdot\{(p+1)(b^2)+(p+1)(2b)^2 \\
&\quad +\ldots+(p+1)(pb)^2-[(b^2)+2(2b)^2+\ldots+p(pb)^2]\} \\
&\quad -\frac{4}{n^2}[(1\cdot 1)ab+(2\cdot 1+2\cdot 2)ab+(3\cdot 1+3\cdot 2+3\cdot 3)ab \\
&\quad +\ldots+(p\cdot 1+p\cdot 2+\ldots+p\cdot p)ab]^2 \\
&= \frac{4a^2b^2}{n^2}\left(\sum_{i=1}^{p}i^3\right)\cdot\left[(p+1)\sum_{i=1}^{p}i^2-\sum_{i=1}^{p}i^3\right] \\
&\quad -\frac{4}{n^2}\left[ab\sum_{i=1}^{p}\frac{i^2(i+1)}{2}\right]^2 \\
&= \frac{4a^2b^2}{n^2}\left\{\left(\sum_{i=1}^{p}i^3\right)\cdot\left[(p+1)\sum_{i=1}^{p}i^2-\sum_{i=1}^{p}i^3\right]\right. \\
&\quad \left.-\left[\frac{1}{2}\left(\sum_{i=1}^{p}i^3+\sum_{i=1}^{p}i^2\right)\right]^2\right\} \\
&= \frac{4a^2b^2}{n^2}\cdot\left\{\frac{p^2(p+1)^2}{4}\cdot\left[(p+1)\frac{p(p+1)(2p+1)}{6}-(\frac{p(p+1)}{2})^2\right]\right. \\
&\quad \left.-\left[\frac{p^2(p+1)^2}{4\cdot 2}+\frac{p(p+1)(2p+1)}{6\cdot 2}\right]^2\right\} \\
&= \frac{4a^2b^2}{n^2}\cdot\frac{p^2(p+1)^2}{4}\cdot\left\{\left[\frac{p(p+1)^2(2p+1)}{6}-\frac{p^2(p+1)^2}{4}\right]\right. \\
&\quad \left.-\left[\frac{p(p+1)}{4}+\frac{(2p+1)}{6}\right]^2\right\} \\
&= a^2b^2\cdot\left[\frac{2p(p+1)^2(2p+1)-3p^2(p+1)^2}{12}-\left(\frac{3p^2+7p+2}{12}\right)^2\right] \\
&= a^2b^2\cdot\left[\frac{p(p+1)^2(p+2)}{12}-\left(\frac{3p^2+7p+2}{12}\right)^2\right] \\
&= \frac{3p^4+6p^3-p^2-4p-4}{144}\cdot a^2b^2
\end{aligned}
\tag{6}
$$

Eq. (4) can be derived from the following equation, where $n = 8n_1$:

$$
\begin{aligned}
\varepsilon^2 &= \frac{1}{n^2}\sum_{i=1}^{n}(x_i-\bar{x})^2\cdot\sum_{i=1}^{n}(x_i'-\bar{x'})^2-\frac{1}{n^2}\Big[\sum_{i=1}^{n}(x_i-\bar{x})\cdot(x_i'-\bar{x'})\Big]^2 \\
&= \frac{1}{(8n_1)^2}(2n_1\cdot 4a^2\cdot 2n_1\cdot 2b^2)-\frac{1}{(8n_1)^2}(2n_1\cdot 2ab)^2=\frac{a^2b^2}{4}
\end{aligned}
\tag{7}
$$

Eq. (5) can be derived from the following equation, where $n = 8n_1$:

$$\begin{aligned}
\varepsilon^2 &= \frac{1}{n^2}\sum_{i=1}^{n}(x_i-\bar{x})^2\cdot\sum_{i=1}^{n}(x_i'-\bar{x'})^2-\frac{1}{n^2}\left[\sum_{i=1}^{n}(x_i-\bar{x})\cdot(x_i'-\bar{x'})\right]^2\\
&=\frac{1}{(8n_1)^2}\cdot 4n_1(2a)^2\cdot[2n_1(k_2a+b)^2\\
&\quad+2n_1(-k_2a+b)^2+4n_1(k_2a)^2]\\
&\quad-\frac{1}{(8n_1)^2}\cdot[2n_1a\cdot(k_2a+b)\\
&\quad+4k_2n_1(a)^2+2n_1a\cdot(k_2a+b)]^2\\
&=\frac{1}{64}\cdot 16a^2\cdot[2\cdot 2((k_2a)^2+b^2)+4(k_2a)^2]\\
&\quad-\frac{1}{64}\cdot[8k_2a^2+4ab]^2\\
&=a^2\cdot[2(k_2a)^2+b^2]-\left[k_2a^2+\frac{ab}{2}\right]^2\\
&\quad=2k_2^2a^4+a^2b^2-k_2^2a^4-\frac{a^2b^2}{4}-k_2a^2ab\\
&=k_2^2a^4-k_2a^3b+\frac{3a^2b^2}{4}\\
&\quad=a^4\cdot\left(k_2^2-\frac{b}{a}k_2+\frac{3b^2}{4a^2}\right)
\end{aligned}\tag{8}$$

Author contributions All authors contributed to the study conception and design. The study was supervised by Tong-Ning Hu and Guang-Yao Feng. Material preparation, data collection, and analysis were conducted by Xiao-Yu Peng and Hao Hu. Formal analysis and investigation were conducted by Xiao-Yu Peng and Jian Pang. Software was contributed by Hao Hu. Resources were provided by Tong-Ning Hu, Jian-Jun Deng, and Guang-Yao Feng. The first draft of the manuscript was written by Xiao-Yu Peng, and all authors commented on and revised previous versions of the manuscript. All authors read and approved the final manuscript.

Data availability The data that support the findings of this study are openly available in Science Data Bank at https://cstr.cn/31253.11.sciencedb.j00186.00762 and https://doi.org/10.57760/sciencedb.j00186.00762.

Declarations

Conflict of interest The authors declare that they have no Conflict of interest.

References

1. S. Sheng, G. Lin, Q. Gu et al., Electron gun for SSRF. Nucl. Sci. Tech. **14**, 20–23 (2003) http://www.nst.sinap.ac.cn/article/id/1633?lang=en
2. L.J. Wang, T. Sen, J.Y. Tang et al., Beam effects and mitigation in a future proton proton collider. Nucl. Sci. Tech. **33**, 130 (2022). https://doi.org/10.1007/s41365-019-0561-y
3. Y.U. Jeong, K.-H. Jang, S. Bae et al., Prospects of a terahertz free-electron laser for field application. J. Korean Phys. Soc. **80**, 367–376 (2022). https://doi.org/10.1007/s40042-022-00428-8
4. T. Hu, Y. Pei, B. Qin et al., Development of a novel thermionic rf electron gun applied on a compact THz-FEL facility. Nucl. Instrum. Meth. Phys. Res. Sect. A **887**, 1–6 (2018). https://doi.org/10.1016/j.nima.2017.12.070
5. C.J. Milne, T. Schietinger, M. Aiba et al., Swissfel: the swiss x-ray free electron laser. Appl. Sci. **7**, 720 (2017). https://doi.org/10.3390/app7070720
6. P. Emma, R. Akre, J. Arthur et al., First lasing and operation of an ångstrom-wavelength free-electron laser. Nat. Photonics **4**, 641–647 (2010). https://doi.org/10.1038/nphoton.2010.176
7. W.A. Ackermann, G. Asova, V. Ayvazyan et al., Operation of a free-electron laser from the extreme ultraviolet to the water window. Nature Photon. **1**, 336–342 (2007). https://doi.org/10.1038/nphoton.2007.76
8. X.J. Wang, X. Qiu, I. Ben-Zvi, Experimental observation of high-brightness microbunching in a photocathode RF electron gun. Phys. Rev. E **54**, R3121–R3124 (1996). https://doi.org/10.1103/PhysRevE.54.R3121
9. S. A. Getty, T. T. King, R. A. Bis et al., Performance of a carbon nanotube field emission electron gun. in SPIE defense + commercial sensing (2007). https://doi.org/10.1117/12.720995
10. A.W. Cross, W. He, A.D.R. Phelps et al., Helically corrugated waveguide gyrotron traveling wave amplifier using a thermionic cathode electron gun. Appl. Phys. Lett. **90**, 253501 (2007). https://doi.org/10.1063/1.2749425
11. X. Gu, Z. Altinbas, S. Badea et al., Stable operation of a high-voltage high-current dc photoemission gun for the bunched beam electron cooler in RHIC. Phys. Rev. Accel. Beams **23**, 013401 (2020). https://doi.org/10.1103/PhysRevAccelBeams.23.013401
12. C. Wang, Z.H. Zhu, Z.G. Jiang et al., Design of a 162.5 MHz continuous wave normal conducting radiofrequency electron gun. Nucl. Sci. Tech. **31**, 110 (2020). https://doi.org/10.1007/s41365-020-00817-3
13. D. Satoh, M. Yoshida, N. Hayashizaki, Development of better quantum efficiency and long lifetime iridium cerium photocathode for high charge electron RF gun. Vacuum **10**, 10–16 (2013) https://accelconf.web.cern.ch/ipac2013/papers/mopfi023
14. H. Chen, L.M. Zheng, B. Gao et al., Beam dynamics optimization of very-high-frequency gun photoinjector. Nucl. Sci. Tech. **33**, 116 (2022). https://doi.org/10.1007/s41365-022-01105-y
15. H. Wang, B. Zeng, Y. Zeng et al., Optimization of quantum current beam modulator based on electron gun. in *2023 IEEE 6th international electrical and energy conference (CIEEC)*, 3179–3183 (2023). https://doi.org/10.1109/CIEEC58067.2023.10165982
16. B.Q. Zeng, T.N. Hu, L.Y. Li et al., Electron beam optimization with application to current quantification. Proc. Autom. Instrum. **43**, 102–112 (2022). https://doi.org/10.16086/j.cnki.issn1000-0380.2021120004. (**in Chinese**)
17. Z. Qin, P. Liu, Y. Peng et al., A grid-controlled thermionic cathode electron gun for new generation CT system. Vacuum Electron. **3**, 51–53 (2020). https://doi.org/10.16540/j.cnki.cn11-2485/tn.2020.03.09
18. T. Asaka, T. Inagaki, T. Magome et al., Low-emittance radio-frequency electron gun using a gridded thermionic cathode. Phys. Rev. Accel. Beams **23**, 063401 (2020). https://doi.org/10.1103/PhysRevAccelBeams.23.063401
19. Y.M. Peng, J.S. Cao, J.H. Chen et al., Milestone progress of the HEPS booster commissioning. Nucl. Sci. Tech. **35**, 16 (2024). https://doi.org/10.1007/s41365-024-01365-w
20. S.C. Wang, D.Y. He, C. Meng et al., Development and simulation of a gridded thermionic cathode electron gun for a high-energy photon source. Nucl. Sci. Tech. **34**, 39 (2023). https://doi.org/10.1007/s41365-023-01195-2

21. G.F. Qu, W.P. Chai, J.W. Xia et al., Two-plane painting injection scheme for bring of HIAF. Nucl. Sci. Tech. **28**, 114 (2017). https://doi.org/10.1007/s41365-017-0260-5
22. J. Wu, X. Li, B. Wu et al., Design and commissioning of a wide-band RF system for CSNS-II rapid-cycling synchrotron. Nucl. Sci. Tech. **35**, 5 (2024). https://doi.org/10.1007/s41365-024-01377-6
23. G.R. Li, S.X. Zheng, H.J. Zeng et al., Design and test of an RF acceleration system loaded with magnetic alloy for the proton synchrotron of the xi'an proton application facility. Nucl. Sci. Tech. **29**, 94 (2018). https://doi.org/10.1007/s41365-018-0434-9
24. H. Chen, Y. Du, W. Gai et al., Surface-emission studies in a high-field rf gun based on measurements of field emission and schottky-enabled photoemission. Phys. Rev. Lett. **109**, 204802 (2012). https://doi.org/10.1103/PhysRevLett.109.204802
25. Y. Zou, H. Li, M. Reiser et al., Theoretical study of transverse emittance growth in a gridded electron gun. Nucl. Instrum. Meth. Phys. Res. A **519**, 432–441 (2004). https://doi.org/10.1016/j.nima.2003.11.183
26. Q.L. Yu, D. Gu, M. Zhang et al., Transverse phase space reconstruction study in shanghai soft X-ray FEL facility. Nucl. Sci. Tech. **29**, 9 (2018). https://doi.org/10.1007/s41365-017-0338-0
27. T. Asaka, H. Ego, H. Hanaki et al., Low-emittance thermionic-gun-based injector for a compact free-electron laser. Phys. Rev. Accel. Beams **20**, 080702 (2017). https://doi.org/10.1103/PhysRevAccelBeams.20.080702
28. T. Hu, Y. Pei, B. Qin et al., Study of beam transverse properties of a thermionic electron gun for application to a compact THz free electron laser. Rev. Sci. Instrum. **85**, 103302 (2014). https://doi.org/10.1063/1.4897481
29. X. Peng, T. Hu, Y. Peng, Optimized design of a thermionic electron gun applied to a high-power FEL injector. in, et al., IEEE 4th China international youth conference on electrical engineering (CIYCEE). IEEE **2023**, 1–6 (2023). https://doi.org/10.1109/CIYCEE59789.2023.10401544
30. C.J. Tan, C.X. Tang, W.H. Huang et al., Beam and image experiment of beam deflection electron gun for distributed X-ray sources. Nucl. Sci. Tech. **30**, 50 (2019). https://doi.org/10.1007/s41365-019-0561-y
31. N. Singh, S.M. Saini, T. Nautiyal et al., Electronic structure and optical properties of rare earth hexaborides RB_6 (R= La, Ce, Pr, Nd, Sm, Eu, Gd). J. Phys. Cond. Matter. **19**, 346226 (2007). https://doi.org/10.1088/0953-8984/19/34/346226
32. P.R. Davis, M.A. Gesley, G.A. Schwind et al., Comparison of thermionic cathode parameters of low index single crystal faces of LaB_6, CeB_6 and PrB_6. Appl. Surf. Sci. **37**, 381–394 (1989). https://doi.org/10.1016/0169-4332(89)90499-6
33. M. Bakr, R. Kinjo, Y. Choi et al., Assessment of thermionic emission properties and back bombardment effects for LaB_6 and CeB_6, in 33rd free electron laser conference Shanghai, China, (2011)
34. K. Kittimanapun, C. Dhammatong, N. Juntong et al., Low emittance thermionic electron gun at SLRI. in *9th Int Part Acc Conf (IPAC 2018), Vancouver, BC, Canada*, 4509–4511 (2018). https://doi.org/10.18429/JACoW-IPAC2018-THPMK088
35. K. Togawa, T. Shintake, T. Inagaki et al., CeB_6 electron gun for low-emittance injector. Phys. Rev. ST Accel. Beams **10**, 020703 (2007). https://doi.org/10.1103/PhysRevSTAB.10.020703
36. F.J. Sacherer, RMS envelope equations with space charge. IEEE Trans. Nucl. Sci. **18**, 1105–1107 (1971). https://doi.org/10.1109/TNS.1971.4326293
37. T. Hu, Y. Pei, G. Feng et al., Conceptual design for a novel pre-injector applied in a high power terahertz free electron laser. Jap. J. Appl. Phys. **57**, 096202 (2018). https://doi.org/10.7567/JJAP.57.096202
38. C. Saisa-ard, S. Rimjaem, Design and beam dynamic simulation of the thermionic RF electron gun with external resonant cavity for transverse emittance reduction. Nucl. Instrum. Meth. Phys. Res. Sect. A **940**, 243–253 (2019). https://doi.org/10.1016/j.nima.2019.06.035
39. X.Y. Zhang, W.M. Pan, G.W. Wang et al., Design of a 325 MHz half wave resonator prototype at IHEP. Chin. Phys. C **40**, 087003 (2016). https://doi.org/10.1088/1674-1137/40/8/087003
40. T.-N. Hu, H.-M. Wang, Y.-F. Zeng et al., Fault locating for traveling-wave accelerators based on transmission line theory. Nucl. Sci. Tech. **34**, 116 (2023). https://doi.org/10.1007/s41365-023-01279-z
41. H. Vennekate, A. Arnold, P. Lu et al., Emittance compensation schemes for a superconducting RF injector. Phys. Rev. Accel. Beams **21**, 093403 (2018). https://doi.org/10.1103/PhysRevAccelBeams.21.093403